Phase-field modeling of dry snow metamorphism

Thomas U. Kaempfer*
Cold Regions Research and Engineering Laboratory, ERDC-CRREL, 72 Lyme Road, Hanover, New Hampshire 03755, USA

Mathis Plapp†
Physique de la Matière Condensée, Ecole Polytechnique, CNRS, 91128 Palaiseau, France
(Received 5 December 2008; published 13 March 2009)

Snow on the ground is a complex three-dimensional porous medium consisting of an ice matrix formed by sintered snow crystals and a pore space filled with air and water vapor. If a temperature gradient is imposed on the snow, a water vapor gradient in the pore space is induced and the snow microstructure changes due to diffusion, sublimation, and resublimation: the snow metamorphoses. The snow microstructure, in turn, determines macroscopic snow properties such as the thermal conductivity of a snowpack. We develop a phase-field model for snow metamorphism that operates on natural snow microstructures as observed by computed x-ray microtomography. The model takes into account heat and mass diffusion within the ice matrix and pore space, as well as phase changes at the ice-air interfaces. Its construction is inspired by phase-field models for alloy solidification, which allows us to relate the phase-field to a sharp-interface formulation of the problem without performing formal matched asymptotics. To overcome the computational difficulties created by the large difference between diffusional and interface-migration time scales, we introduce a method for accelerating the numerical simulations that formally amounts to reducing the heat- and mass-diffusion coefficients while maintaining the correct interface velocities. The model is validated by simulations for simple one- and two-dimensional test cases. Furthermore, we perform qualitative metamorphism simulations on natural snow structures to demonstrate the potential of the approach.

DOI: 10.1103/PhysRevE.79.031502 PACS number(s): 64.70.Hz, 44.30.+v, 44.35.+c

I. INTRODUCTION

Snow is a porous material consisting of ice grains that are connected by bonds, air-filled pore space, small amounts of impurities, and sometimes liquid water. The complex microstructure of this material changes with time due to sintering processes, which lead to a redistribution of matter. This evolution is driven by the fact that interfaces and grain boundaries are not in their equilibrium configurations and is favored by the high temperatures close to the melting point of water that always prevail under terrestrial conditions. Transport mechanisms include diffusion along grain boundaries and surfaces as well as diffusion of water vapor through the pore space, accompanied by sublimation and resublimation (vapor to solid phase change). In a snowpack subjected to a temperature gradient, a water vapor concentration gradient in the pore space is induced. This leads to enhanced water vapor diffusion along the gradient that dominates other processes and to a more rapid evolution of the snow microstructure. These continuous changes of the snow microstructure are called snow metamorphism, and in particular temperature gradient metamorphism in the latter case.

The snow microstructure directly influences several snowpack properties, including mechanical properties used in avalanche forecasting [1], chemical composition associated with the interpretation of ice core data [2], and thermophysical properties important for modeling the energy balance of snow-covered landscapes [3,4]. These properties evolve simultaneously with the snow microstructure during metamorphism. The link between heat transport and metamorphism is particularly strong. On the one hand, heat flow through snow induces mass flow and an evolution of the ice and pore network as described above; on the other hand, the microstructure influences heat flow since the heat conductivities of ice and air are very different, and since heat can also be redistributed by phase-change processes and water vapor transport in the pore space (Fig. 1).

The strong link between snow microstructure and physical properties was recognized early on, and there is a vast body of experimental and theoretical work on snow metamorphism; we refer to Arons and Colbeck [5] for a review. The most modern observational techniques are based on computed x-ray microtomography (μ-CT) [6–9], and allow for nondestructive observations of metamorphosing snow at a resolution of approximately 10 μm. The images shown in Fig. 1 were taken from a cylindrical snow sample of height 2 cm and diameter 5 cm which resided in a specially constructed snow breeder inside a Scanco μ-CT80 desktop computer tomograph [9]. Both the average temperature and the temperature gradient were controlled. Difference images between successive scans (Fig. 1, center) were used to study the sublimation and resublimation processes.

On the modeling side, most existing work deals with simplified geometries, from serial and parallel plates over Maxwellian models with dispersed spherical particles to combinations of both. One of the most recent approaches considers heat and mass fluxes within a network of spherical grains bonded by concave necks and was applied both to isothermal and temperature-gradient metamorphism [10]. Some models are tailored to specific problems, for example, to predict the evolution of the specific surface area during metamorphism

*thomas.kaempfer@usace.army.mil
†mathis.plapp@polytechnique.fr

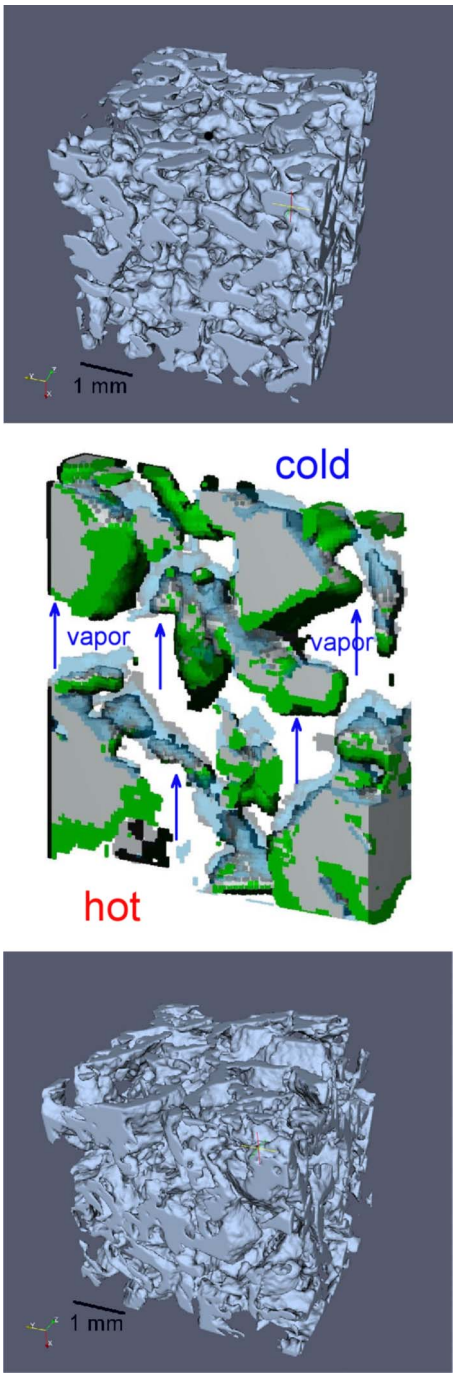

FIG. 1. (Color online) Metamorphosing snow imaged by computed x-ray microtomography: Fine grained snow (top) evolves towards a coarser and more faceted structure (bottom) when submitted to a temperature gradient (here $\nabla T \cong 50$ K/m, $T \cong -3.4\,^{\circ}$C, time 10 days). Due to the temperature gradient, a water vapor gradient arises in the pore space that drives mass flow (center); blue represents sublimated, green freshly grown ice during one day, as observed by taking the difference image between two successive tomography scans.

[11]. Such simple models or fits to experimental data were used to develop parametrizations of snow metamorphism in terms of quantifiable geometric quantities such as grain and bond sizes and forms [12,13]. However, questions remain

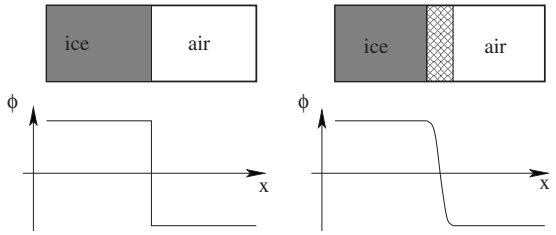

FIG. 2. Sharp interface (left) and diffuse interface (right) with the phase-field function ϕ.

with respect to the range of validity of parametrizations and, more fundamentally, the relative importance of the processes governing metamorphism. Only a few modeling attempts that can assimilate more realistic microstructures exist. Christon *et al.* [14] developed an adaptive finite-element method to solve the coupled two-phase heat- and mass-conservation problem, including phase change, on an *a priori* arbitrary microstructure. However, due to the choice of the numerical method, no topological changes of the microstructure are allowed in this model. This prohibits the application to real snow microstructures and limits the computations to relatively simple artificial ice lattices and short time scales. More recently, Flin *et al.* [15] considered curvature-driven snow metamorphism and simulated it on three-dimensional tomographic snow structures. The model is based on an analytically obtained growth and sublimation law for the ice phase, assumes infinitely fast water vapor diffusion in the pore space, and neglects any other driving forces than curvature differences at the ice-air interfaces. In a second approach [16], the same authors proposed a model where the vapor diffusion in the pore space is the main limiting mechanism. By computing diffusive fluxes combined with an atomistic approach for grain growth and sublimation they predicted regions of potential facetted growth and rounding sublimation within tomographic snow structures subjected to low temperature gradients. Also using μ-CT images as structural input, Kaempfer *et al.* [17] studied heat transfer through snow. At present, no numerical model operates at similar length scales and microstructural complexity as those provided by μ-CT experiments while at the same time containing more complete fundamental physics. This would be highly desirable to study metamorphism in detail; the present work tries to fill in this gap.

The phase-field method is ideally suited for this task, since it is capable of solving the fully coupled heat- and mass-transfer problem with phase change and can easily handle topological changes. The central idea of this method is to avoid the explicit tracking of the ice-air interface by the introduction of an additional field. This so-called phase field ϕ varies smoothly from one value in the solid (ice) to another value in the vapor (air) across a spatially diffuse interface region of thickness W (Fig. 2). The time evolution of the microstructure is then described by an equation of motion for the phase field. This converts the sharp-interface tracking problem to that of solving a system of coupled partial differential equations, which governs the evolution of the phase and diffusion fields; the latter is much easier to handle numerically. Phase-field methods have been extensively used to

study interfacial pattern formation phenomena in solidification and solid-state phase transformations (see the reviews by Boettinger *et al.* [18] and Chen [19]), as well as in many other fields.

In the present paper, we develop and test a phase-field model for snow metamorphism. It solves the coupled heat- and mass-transfer problem with phase change in an arbitrary snow microstructure. We consider diffusive heat fluxes through the ice matrix and pore space, water vapor diffusion across the pores, and (re)sublimation of ice or water vapor at the ice-air interfaces, depending on undersaturation or supersaturation above the interface. These nonequilibria can be due to local temperature gradients, since the water vapor saturation pressure in air is strongly temperature dependent, but also contain capillary (curvature) and kinetic effects. Other phenomena, in particular grain boundary diffusion or the anisotropies created by the crystal structure, will be neglected.

The problem considered in the literature that is most closely related to the present work is the solidification of alloys, where transport of both heat and matter needs to be treated. Therefore, our phase-field formulation is based on models that have been developed in the context of solidification. An important point that needs to be addressed if accurate results are desired is how the parameters of the phase-field model have to be chosen in order to reproduce a given sharp-interface problem. In solidification, this problem has been studied in detail by the technique of matched asymptotic expansions, in which the thickness W of the diffuse interface is treated as a small parameter. In the so-called sharp-interface limit [20,21], W tends to zero, and the transport fields (e.g., temperature) are assumed to be constant through the interface. In the thin-interface limit, developed later [22,23], W is small but finite, and the spatial variations of the transport fields through the interface are taken into account. The thin-interface limit is more precise, but has so far been worked out only for a few specific simple models. Snow metamorphism is not well described by any of those models; however, as will be discussed in detail below, the intrinsic properties of the ice-vapor interface (in particular its slow kinetics) and the experimental conditions we wish to simulate justify the use of the simpler sharp-interface limit.

An additional problem, not present in solidification, arises for simulations of snow metamorphism because two hugely different time scales are present in the problem: the time a water molecule needs to diffuse across a pore is typically eight to ten orders of magnitude smaller than the time a pore needs to migrate by a distance of once its size. Fortunately, this problem can be solved by a suitable rescaling of the physical parameters that amounts to reducing the diffusion constants (which implies that larger time steps can be used) while maintaining the correct interface velocities. A speedup of the simulations by several orders of magnitude can be achieved without appreciably altering the simulation results, such that realistic evolutions of complex two- and three-dimensional snow microstructures on the time scale of hours to days can be simulated in reasonable computational time.

The remainder of the paper is organized as follows. In Sec. II, we first summarize the main physical features of snow metamorphism in a sharp-interface framework and give estimates for the values of the interfacial properties that appear in the model. Next, we introduce the corresponding phase-field formulation and deduce its properties from the analogy with the well-known phase-field models for solidification. This allows us to relate the phase-field and the sharp-interface formulations. Finally, we discuss the method for accelerating the numerical simulations. In Sec. III, we validate the method by performing simulations of simple one- and two-dimensional model problems with artificial microstructures. Moreover, we carry out snow metamorphism simulations operating on two-dimensional slices or on the full three-dimensional natural snow microstructures obtained by μ-CT. Finally, we discuss the model, results, and perspectives (Sec. IV) followed by the conclusion in Sec. V.

II. MODEL

A. Physics of ice sublimation

Nonisothermal dry snow metamorphism is governed by heat- and mass-conservation laws in the two-phase material snow consisting of ice (properties with subscript i) and pores containing air and water vapor (properties with subscript a), together with the motion of the ice-air interfaces due to phase change. For simplicity, we suppose that the heat conductivities $\kappa_{i,a}$ and the heat capacities per unit volume $C_{i,a}$ of both phases are constant. Note that all the notations with typical values for the problem at hand are summarized in Table I. Constant parameters are justified since we are interested in simulations of snow metamorphism on rather small spatial domains with size of the order of millimeters, which implies that the temperature range within the sample is small even though our snow will be subjected to a global temperature gradient: the temperature-induced variations of the physical properties are small (on the order of 1%) for a temperature range of several degrees. Hence, we evaluate them at a fixed reference temperature T_0. Moreover, we will assume the transport properties of air to be those of dry air, since the humidity ratio at saturation $x_s \ll 1$ and we expect the air in the pore space to be close to saturation.

Note, however, that the variation of x_s with temperature is large and cannot be neglected; it is the physical origin of the coupling between temperature gradient and vapor diffusion. We have

$$x_s(T) = \frac{R_{da}}{R_v}\frac{P_{vs}(T)}{P_a - P_{vs}(T)} \cong 0.62\frac{P_{vs}(T)}{P_a - P_{vs}(T)}, \tag{1}$$

where R_{da} and R_v are the individual gas constants [48] of dry air and water vapor, respectively, P_a is the atmospheric pressure supposed to be constant, and P_{vs} is the saturation vapor pressure of water vapor over ice. The latter varies strongly with temperature and can be approximated by the formula [24]

$$P_{vs}(T) = \exp\left(\sum_{j=0}^{4} K_j T^{j-1} + K_5 \ln T\right), \tag{2}$$

where $\{K_j\}_{j=0,1,\ldots,5}$ are fitting coefficients listed in Table I.

TABLE I. Notations and numerical values of parameters. Unless stated otherwise, the constants used for the phase-field computations were evaluated at a reference temperature of $T_0=-10\ ^\circ\mathrm{C}$, respectively, 263 K.

Symbol	Description	Value, unit	Reference
a	mean intermolecular spacing in ice	3.19×10^{-10} m	[30]
d_0	capillary length	1.3×10^{-9} m	
k	Boltzmann's constant	1.38×10^{-23} J K^{-1}	
m	mass of a water molecule	$0.018/6.02\times10^{23}=2.99\times20^{-26}$ kg	[30]
$\hat{n}$	unit vector normal to the interface and pointing from the ice to the air		
t, t_D, t_n	time, characteristic water vapor diffusion time, characteristic interface migration time	$-$, $\sim10^{-4}$, $\sim10^{5}$ s	
u, u_{eq}	dimensionless concentration field, at equilibrium		
v_n	normal interface velocity	$\sim10^{-9}$ m s^{-1}	
x_s	specific humidity ratio of air at saturation	kg/kg	
C_i, C_a	specific heat capacity of ice, (dry) air per volume	1.8×10^{6}, 1.4×10^{3} J m^{-3} K^{-1}	[30,47]
D	water diffusion coefficient, equal D_v in the air, equal zero in the ice	m^2 s^{-1}	
D_v, D_v^{STP}	water vapor diffusion coefficient in the air, at standard pressure and temperature	2.178×10^{-5} m^2 s^{-1}	[25]
$\{K_j\}_{j=0,1,\ldots,5}$	fitting coefficients for saturation vapor pressure and (the units for temperature and pressure are K and Pa, respectively)	$\{-0.5865\times10^{4}$, 0.2224×10^{2}, 0.1375×10^{-1}, -0.3403×10^{-4}, 0.2697×10^{-7}, $0.6918\}$	[24]
L_{sg}	latent heat of sublimation of ice per volume	2.60×10^{9} J m^{-3}	[26]
P, P_a, P^{STP}	pressure, atmospheric pressure, standard pressure	1.01325×10^{5} Pa	
P_{vs}	saturation pressure of water vapor over ice	Pa	[24]
R_{da}, R_v	individual gas constants of dry air and water vapor	286.9, 461.5 J Kg^{-1} K^{-1}	
T, T^{STP}	temperature, standard temperature	273.15 K	
W	interface thickness	m	
α	condensation coefficient	$10^{-3}<\alpha<10^{-1}$	[31]
β	interface kinetic coefficient	$3\times10^{4}<\beta<3\times10^{6}$, in simulations $\beta=5.5\times10^{5}$ s m^{-1}	
γ	interfacial free energy of ice	1.09×10^{-1} J m^{-2}	[26]
κ_i, κ_a	heat conductivity of ice, (dry) air	2.29, 0.02 W m^{-1} K^{-1}	[47]
λ	phase-field coupling constant related to the capillary length		
ν	exponent for temperature dependence of water vapor diffusion coefficient	1.81	[25]
ϕ	phase field		
ρ_i, ρ_a	density of ice, (dry) air	918.9, 1.341 kg m^{-3}	[47]
ρ_v	water (vapor) concentration	kg m^{-3}	
ρ_{vs}	equilibrium water vapor concentration at saturation	$\sim10^{-3}$ to 10^{-2} kg m^{-3}	[24]
σ	normalized supersaturation		
τ	phase-field relaxation time	s	
$\mathcal{K}$	interface curvature	m^{-1}	

We use the above approximation together with Eq. (1) to define the equilibrium water vapor mass density at saturation in the air ρ_{vs} by

$$\rho_{vs}(T) = \rho_a x_s(T), \tag{3}$$

where ρ_a is the mass density of dry air. Two other physical properties are needed and are supposed to be constant: the water vapor diffusion coefficient in air D_v and the latent heat of sublimation per unit volume L_{sg}. The former can be computed based on the kinetic theory of a binary gas and will be approximated for $T=T_0$ and $P=P_a$ using [25]

$$D_v(T,P) = D_v^{\mathrm{STP}} \frac{P^{\mathrm{STP}}}{P} \left(\frac{T}{T^{\mathrm{STP}}} \right)^{\nu}, \tag{4}$$

where T^{STP} and P^{STP} are the standard temperature and pressure (STP), D_v^{STP} is the water vapor diffusion coefficient at STP, and the exponent $\nu=1.81$ is supposed to be constant. For the latent heat L_{sg} we use a constant value taken from [26].

As mentioned above, we need to take into account fluxes of energy and matter. For the latter, we will suppose that transport of matter is limited to diffusion in the pore space and that the density of the ice is constant and equal to ρ_i. The conservation equation for water vapor in the pore space is deduced from Fick's law and reads

$$\frac{\partial \rho_v}{\partial t} = \nabla \cdot (D_v \nabla \rho_v). \tag{5}$$

At an ice-air interface, mass conservation implies that the motion of the interface is linked to the diffusion flux in the pore by the Stefan condition

$$D_v \hat{n} \cdot \nabla \rho_v = (\rho_i - \rho_v) v_n \cong \rho_i v_n, \tag{6}$$

where ρ_v is the vapor density in the pore space (adjacent to the interface), $\hat{n}$ is the unit normal vector to the interface pointing from the solid into the pore, and v_n is the normal interface velocity, defined as positive when the ice grows. The last approximation in Eq. (6) is obtained by setting $\rho_i - \rho_v \cong \rho_i$ since $\rho_i \gg \rho_v$.

Energy can be transported in two ways: either by direct heat conduction through ice and air, or it can be carried through the pore space in the form of latent heat of sublimation by the diffusing water vapor. Again neglecting convection, heat conduction in the ice and the pore space is governed by

$$C_i \frac{\partial T_i}{\partial t} = \nabla \cdot (\kappa_i \nabla T_i), \quad C_a \frac{\partial T_a}{\partial t} = \nabla \cdot (\kappa_a \nabla T_a). \tag{7}$$

At an ice-air interface, the conservation of energy implies a second Stefan condition

$$\kappa_i \hat{n} \cdot \nabla T|_i = \kappa_a \hat{n} \cdot \nabla T|_a + L_{sg} v_n, \tag{8}$$

where the source term on the right-hand side is due to sublimation and resublimation. Note that this equation can also be rewritten by combining it with Eq. (6) as

$$\kappa_i \hat{n} \cdot \nabla T|_i = \kappa_a \hat{n} \cdot \nabla T|_a + \frac{L_{sg}}{\rho_i} D_v \hat{n} \cdot \nabla \rho_v. \tag{9}$$

The problem is closed by specifying boundary conditions for the temperature and density fields. For the temperature, we suppose that it is continuous across the interface,

$$T_i = T_a. \tag{10}$$

The vapor density satisfies a generalized Gibbs-Thomson boundary condition

$$\rho_v = \rho_{vs}(T)(1 + d_0 \mathcal{K} + \beta v_n), \tag{11}$$

where d_0 is the capillary length, $\mathcal{K}$ is the interface curvature (positive for a convex domain occupied by ice), and β is the kinetic coefficient.

The quantities d_0 and β require comments. In fact, the problem has been formulated here in analogy to the problem of solidification, where d_0 and β are standard and well-known quantities. For the sublimation and resublimation of ice, knowledge is far more limited, and neither experiments nor models have been able so far to fully elucidate these processes, in particular the kinetic aspects. The complexity of the problem becomes apparent, for example, in the crystal growth habit diagram of Kobayashi [27], which shows a complex dependence of the growth shape on temperature and supersaturation. A review of the different aspects of snow crystal growth was recently given by Libbrecht [28], and sublimation of ice crystals was studied by Nelson [29]. A complete treatment of the interface dynamics is yet out of reach and some simplifications are needed within the present work. In particular, we will assume both d_0 and β to be constant and isotropic. The possibility of relaxing these hypotheses in the future will be discussed later.

Consider first the capillary length d_0, which defines the dependence of the chemical potential at the ice-air interface on the curvature and is linked to the surface free energy of the interface. At a given temperature T, the saturation water vapor pressure $P_{vs}(\mathcal{K})$ above an ice surface with curvature $\mathcal{K}$ is related to the saturation pressure over a flat surface P_{vs}^0 by the Gibbs-Thomson relation

$$\frac{P_{vs}(\mathcal{K})}{P_{vs}^0} = \exp\left(\frac{\gamma a^3 \mathcal{K}}{kT} \right) = e^{d_0 \mathcal{K}}, \tag{12}$$

where γ is the interfacial free energy, a is the mean intermolecular spacing in the ice, k is Boltzmann's constant, and

$$d_0 = \frac{\gamma a^3}{kT}. \tag{13}$$

Linearizing Eq. (12) around $\mathcal{K}=0$ leads to $P_{vs}(\mathcal{K}) \cong P_{vs}^0(1 + d_0 \mathcal{K})$. Using Eqs. (1) and (3) and approximating $P_{vs}/(P_a - P_{vs}) \cong P_{vs}/P_a$ since $P_a \gg P_{vs}$, the curvature term of Eq. (11) follows. With γ the interface free energy between ice and water vapor [26], noting that ice contains 3.07×10^{28} molecules per unit volume [30] to determine a^3, and at $T=263$ K, we estimate

$$d_0 \sim 10^{-9}\ \mathrm{m}. \tag{14}$$

Note that such a small d_0 implies that the influence of interface curvature on the water vapor pressure and chemical potential is very small for snow grains which are expected to have radii of the order of 0.1 mm. Nevertheless, the *differ-*

ence of local curvatures between different parts of the interface provides a driving force for sublimation and resublimation that cannot be neglected.

Let us now turn to the attachment kinetics and to the kinetic coefficient β. Attachment kinetics in ice are usually studied by the means of the condensation coefficient α. However, experiments without systematic errors are sparse [31] and as a consequence experimental values of α are widely dispersed and only partially reliable. The fact that the surface structure of pure ice, even at equilibrium, is very complex near the melting point and might include a quasiliquid layer [32,33] not only presents a challenge for the experiments but also makes theoretical or numerical estimates difficult. For the moment, our goal is thus only to estimate the order of magnitude of β, remembering that a more realistic estimate for β and in particular its anisotropic variation will be necessary in the future to be able to simulate snow metamorphism more realistically.

For an ice crystal growing from water vapor, we can relate the growth velocity normal to the surface to the supersaturation in terms of the Hertz-Knudsen equation [28]

$$\rho_i v_n = \alpha \sqrt{\frac{kT}{2\pi m}} [\rho_v - \rho_{vs}(T)], \tag{15}$$

where m is the mass of a water molecule. The term $\sqrt{kT/(2\pi m)}$ can be interpreted as the thermal velocity of the water molecules, $\rho_v - \rho_{vs}(T)$ is the supersaturation representing the excess of impinging molecules with respect to the equilibrium situation, and the condensation coefficient α is the fraction of the attempts to join the crystal structure that is successful. Inverting Eq. (15) to obtain ρ_v and comparing to Eq. (11) leads to

$$\beta = \frac{1}{\alpha}\frac{\rho_i}{\rho_{vs}}\sqrt{\frac{2\pi m}{kT}} \cong \frac{1}{\alpha} 3.1 \times 10^3 \text{ s m}^{-1}, \tag{16}$$

where for the estimate we have set $T=263$ K and computed ρ_{vs} using Eq. (3). From the most recent ice crystal growth rate experiments by Libbrecht [31], the condensation coefficient is believed to have values between $10^{-3} < \alpha < 10^{-1}$, which leads to an approximate kinetic coefficient β of

$$3 \times 10^4 \text{ s m}^{-1} < \beta < 3 \times 10^6 \text{ s m}^{-1}. \tag{17}$$

For the discussion of the phase-field model presented below it will be important to note that this kinetic coefficient is very large when compared to typical kinetic coefficients for solidification. This is due to the fact that the crystal grows from a very dilute phase; indeed, the ratio ρ_i/ρ_{vs} in Eq. (16) is of the order 5×10^5 while it would be of the order unity for growth from a liquid phase.

For the subsequent development of the phase-field model, it is useful to define a dimensionless concentration field in the pores. Two different choices are possible. In the field of crystal growth from vapor or from solution, it is customary to work with the supersaturation

$$\sigma = \frac{\rho_v - \rho_{vs}}{\rho_{vs}}. \tag{18}$$

In terms of this variable, the Stefan condition for mass transport and the Gibbs-Thomson condition at the interface read, respectively,

$$v_n = \frac{\rho_{vs}}{\rho_i} D_v \hat{n} \cdot \nabla \sigma, \tag{19}$$

$$\sigma = d_0 \mathcal{K} + \beta v_n. \tag{20}$$

A problem for our treatment of snow metamorphism arises, however, because the temperature is not constant, and hence ρ_{vs} varies from point to point. An alternative is to use a definition that is analogous to the definition of the dimensionless supercooling or the dimensionless supersaturation in solidification,

$$\tilde{u} = \frac{\rho_v - \rho_{vs}}{\rho_i} = \frac{\rho_{vs}}{\rho_i}\sigma. \tag{21}$$

Since we have assumed ρ_i independent of temperature, the only place where temperature dependence remains in this expression is in the offset in the numerator. If we choose a reference temperature T_0 for this offset and define

$$u = \frac{\rho_v - \rho_{vs}(T_0)}{\rho_i}, \tag{22}$$

the Stefan and Gibbs-Thomson boundary conditions can be rewritten as

$$v_n = D_v \hat{n} \cdot \nabla u, \tag{23}$$

$$u = u_{\text{eq}}(T) + d_0' \mathcal{K} + \beta' v_n, \tag{24}$$

with $u_{\text{eq}}(T) = [\rho_{vs}(T) - \rho_{vs}(T_0)]/\rho_i$,

$$d_0' = d_0 \frac{\rho_{vs}}{\rho_i} = \frac{\gamma a^3}{kT}\frac{\rho_{vs}}{\rho_i} \tag{25}$$

and

$$\beta' = \beta \frac{\rho_{vs}}{\rho_i} = \frac{1}{\alpha}\sqrt{\frac{2\pi m}{kT}}. \tag{26}$$

In the last expression for the capillary length in Eq. (25), there appear three temperature-dependent quantities: the surface free energy γ, the ratio $a^3/(kT)$, and the equilibrium vapor concentration ρ_{vs}; the capillary length itself is therefore a temperature-dependent quantity. As mentioned before, we need to retain the temperature dependence of ρ_{vs} in the boundary conditions, since this creates the main driving force for mass redistribution; this is the origin of the term $u_{\text{eq}}(T)$ in Eq. (24). In contrast, the capillary term is generally a small correction to this main driving force. Furthermore, whereas the temperature variations are small on the scale of a microstructural feature, the local variations of curvature can be large. Therefore, the spatial variations of the capillary term that can drive local mass currents arise mainly from the local variations in curvature, such that we can safely replace the temperature-dependent capillary length by its value at the

reference temperature T_0. As for the kinetic coefficient, its temperature dependence arises from the square root term only, which will only induce very small variations over the temperature range considered here; we will therefore also take a constant value for β'.

B. Phase-field formulation

Consider now a phase-field function ϕ which distinguishes between solid (ice) for $\phi=1$ and gas (air) for $\phi=-1$ but varies continuously across an ice-air interface. We use ϕ to define physical parameters everywhere in space by a continuous interpolation of the bulk values. The heat conductivity is defined by

$$\kappa(\phi) = \kappa_i \frac{1+\phi}{2} + \kappa_a \frac{1-\phi}{2}, \tag{27}$$

the heat capacity by

$$C(\phi) = C_i \frac{1+\phi}{2} + C_a \frac{1-\phi}{2}, \tag{28}$$

and the chemical diffusion coefficient for water

$$D(\phi) = D_v \frac{1-\phi}{2}, \tag{29}$$

where we have implicitly assumed no mass diffusion in the ice. Moreover, we define a continuous water concentration, which is equal to the constant ice density ρ_i in the solid, by

$$\rho(\phi) = \rho_i \frac{1+\phi}{2} + \rho_v \frac{1-\phi}{2}. \tag{30}$$

Finally, we postulate that the continuous equilibrium water concentration through a diffuse ice-air interface, i.e., equilibrium water vapor concentration in the air and ice density in the solid, is given by

$$\rho_{\mathrm{eq}}(\phi,T) = \rho_i \frac{1+\phi}{2} + \rho_{vs}(T) \frac{1-\phi}{2}. \tag{31}$$

This amounts to supposing that, at equilibrium, the air in the pore space is saturated with water vapor. Then, the variable u, which was defined in the preceding subsection only in the pores, can be extended to the whole system by defining

$$u = \frac{\rho(\phi) - \rho_{\mathrm{eq}}(\phi,T_0)}{\rho_i}. \tag{32}$$

With the additional approximation that $\rho_i - \rho_{vs}(T) \cong \rho_i = \text{constant}$ [since $\rho_i \gg \rho_{vs}(T)$, $\forall T$] we note that u is constant and equal to $u_{\mathrm{eq}}(T) = [\rho_{vs}(T) - \rho_{vs}(T_0)]/\rho_i$ through an equilibrium interface at a given temperature T. Because of the latter property, the variable u is equivalent to a dimensionless chemical potential.

With the above hypotheses and notations the snow metamorphism model reads

$$\tau \frac{\partial \phi}{\partial t} = W^2 \nabla^2 \phi + (\phi - \phi^3) + \lambda [u - u_{\mathrm{eq}}(T)](1-\phi^2)^2, \tag{33}$$

$$C(\phi) \frac{\partial T}{\partial t} = \nabla [\kappa(\phi) \nabla T] + \frac{L_{sg}}{2} \frac{\partial \phi}{\partial t}, \tag{34}$$

$$\frac{\partial u}{\partial t} = \nabla [D(\phi) \nabla u] - \frac{1}{2} \frac{\partial \phi}{\partial t}, \tag{35}$$

where W is the interface thickness, τ is the phase-field relaxation time, and λ is a dimensionless coupling constant.

These equations represent phase change, heat transport, and mass transport, respectively. Equation (33) is the usual evolution equation of the phase-field model, which can be obtained by minimizing a free energy functional: the first and second terms on the right-hand side are the derivatives of a square gradient and a double-well potential term, respectively. Together, these terms generate bulk phases where $\phi = \pm 1$, separated by diffuse interfaces of width W. The term proportional to λ represents the driving force for the phase transition. Indeed, for $u > u_{\mathrm{eq}}(T)$ (supersaturated vapor) this term is positive, which means that the solid is the favored phase. The factor $(1-\phi^2)^2$ restricts the action of this driving force to the interface regions. Equation (35) describes the transport of mass. The source term on the right-hand side is due to the (re)sublimation processes. Indeed, to construct the solid, water vapor has to be consumed; the prefactor $1/2$ is due to the fact that the difference between the bulk values of the phase field is equal to 2. Finally, Eq. (34) describes the transport of energy. For justifying the latent heat term, we follow Borcia and Bestehorn [34] and first combine Eqs. (34) and (35) to get

$$C(\phi) \frac{\partial T}{\partial t} = \nabla [\kappa(\phi) \nabla T] + L_{sg} \left(\nabla (D(\phi) \nabla u) - \frac{\partial u}{\partial t} \right). \tag{36}$$

When the interface evolution is slow, such that a sharp-interface limit can be performed, the time derivatives can be neglected, and the Stefan condition for the energy conservation (9) can be obtained by first integrating the remaining terms along the coordinate normal to the interface and then evaluating the gradients on both sides of the interface, taking into account that $\nabla u = 0$ in the ice and $\nabla u = \nabla \rho_v / \rho_i$ in the air.

C. Relation between phase-field and sharp-interface parameters

As mentioned in the Introduction, the proof that the phase-field model indeed reproduces the desired sharp interface problem has to be deduced from matched asymptotic expansions. This procedure also yields the relations between the parameters of the phase-field model and the quantities that appear in the sharp-interface formulation. The technique of matched asymptotics relies on the separation of scales between the small thickness of the diffuse interfaces and the length scales of the microstructural pattern (radii of curvature, diffusion lengths). This provides a small parameter for a perturbation expansion $\epsilon = W/l$, where W is the interface thickness and l a scale of the pattern. A complete development of this expansion for the model given above is beyond the scope of this paper. However, all that is needed for a

satisfactory treatment of dry snow metamorphism can be deduced by analogy with the established results on phase-field models for solidification.

In fact, if we would suppose the diffusion coefficient $D(\phi)$ constant and equal to D in both phases, the phase-field equation (33) together with the diffusion equation (35) for u would map onto the classical phase-field formulation for the solidification of a pure substance by identifying D with the thermal diffusion coefficient and u with the dimensionless temperature. In the so-called sharp-interface limit, in which the small parameter $\epsilon \to 0$, this phase-field formulation reduces to the standard Stefan problem given by a diffusion equation $\partial_t u = D\nabla^2 u$, valid in both phases, and a Stefan and Gibbs-Thomson interface condition analogous to Eqs. (23) and (24). Moreover, the basic microscopic parameters of the phase-field model relate to the capillary length and kinetic coefficient by [20,21]

$$d_0' = a_1 \frac{W}{\lambda}, \tag{37}$$

$$\beta' \equiv \beta_0' = a_1 \frac{\tau}{W\lambda}, \tag{38}$$

where $a_1 = (5/8)\sqrt{2}$. For a given d_0' and β', a choice of the simulation parameter W (the interface width) then fixes uniquely the parameters λ and τ.

In order to obtain the above result, it is necessary to assume that the diffusion field u is constant through the interface. However, in numerical simulations, the interface thickness is necessarily finite and therefore u is not strictly constant. Taking into account these variations in the so-called thin-interface limit, where W is required to be small with respect to the scale of the solidification pattern l but remains finite [22,23], yields the same relation for d_0' but a new expression for the kinetic coefficient that reads

$$\beta' = a_1 \left(\frac{\tau}{W\lambda} - a_2 \frac{W}{D} \right), \tag{39}$$

where a_1 is the same constant as before and a_2 is a second constant of order unity. For the purpose of the present paper, it is useful to restate this result in a slightly different way. Suppose that we have (incorrectly) chosen the phase-field parameters according to the sharp-interface limit; how large is the error we have made? Equation (39) can be rewritten to yield

$$\beta' = \beta_0' \left(1 - a_1 a_2 \frac{W}{D\beta_0'} \right). \tag{40}$$

Since we have identified β_0' with the physical kinetic coefficient, the product $D\beta_0'$ (which has the dimension of a length) is a constant specific to the considered material; as long as $W \ll D\beta_0'$, the corrections due to the variations of the diffusion field u through the interface are negligible.

The same fact can be stated in yet another way. For a given kinetic coefficient β_0', the average dimensionless supersaturation is $\bar{u} \sim \beta_0' v_n$. The variations of the supersaturation through the interface Δu are of the order $\Delta u \sim W v_n / D$, which is the ratio of interface thickness to diffusion length; this can either be obtained from the asymptotic analysis by Karma and Rappel [22,23] or from simple dimensional arguments. As long as $\Delta u \ll |\bar{u}|$, the corrections due to the supersaturation variations within the interface can be neglected. This leads to the same criterion as above.

So far, we have supposed the diffusion coefficient D to be constant and equal in both phases. When diffusion becomes asymmetrical, the use of a mesoscopic W additionally magnifies several nonequilibrium effects at the interface. For the solidification of a pure material, these effects were first characterized in detail by Almgren [35] and include (i) a temperature jump across the interface, (ii) a modification of the heat conservation associated with the local increase of arclength of a moving curved interface, called interface stretching, and (iii) surface diffusion along the arclength of the interface. In the analogous problem of isothermal alloy solidification, effect (i) corresponds to a jump in the chemical potential, linked to the physical but artificially enhanced phenomenon of solute trapping. A solution to eliminate these spurious effects in the special case of the so-called one-sided model, in which the solute diffusivity vanishes in the solid, consists in modifying the equation for the solute current by adding a so-called antitrapping current that is nonvanishing only within the diffuse interface and counteracts these effects [36,37]. As a result, this model satisfies the same relations for the parameters as the symmetric model. Using the same technique of the antitrapping current, Ramirez *et al.* [38] extended the model to the problem of thermosolutal solidification of a dilute binary alloy with symmetric thermal and one-sided solutal diffusivities; this is the model most closely related to our snow metamorphism formulation. Here, the thin-interface limit leads to a modified equation for β', where the correction added to the sharp-interface limit is now dependent on the heat and solute conductivities

$$\beta' = a_1 \left(\frac{\tau}{W\lambda} - a_2 \frac{W}{\alpha_T} - a_3 \frac{W}{D_v} \right), \tag{41}$$

where, in addition, the value of a_3 depends on the local interface temperature, and we have denoted the thermal diffusion coefficient by α_T.

To obtain a complete analysis of our model, we would need to follow the lines of the works cited above. A simpler way to make progress is to observe that from simple dimensional arguments, the thin-interface corrections in the kinetic coefficient must scale as W/α_T and W/D_v, where in our case $\alpha_T(\phi) = \kappa(\phi)/C(\phi)$. The requirement that the sharp-interface limit be a good approximation for the behavior of our model then yields the conditions

$$\frac{W}{\kappa_i/C_i} \ll \beta_0', \quad \frac{W}{\kappa_a/C_a} \ll \beta_0', \quad \frac{W}{D_v} \ll \beta_0', \tag{42}$$

or, using Eq. (26) for β_0' and rearranging terms,

$$W \ll \frac{\kappa_i}{C_i}\frac{\rho_{vs}}{\rho_i}\beta_0, \quad W \ll \frac{\kappa_a}{C_a}\frac{\rho_{vs}}{\rho_i}\beta_0, \quad W \ll D_v \frac{\rho_{vs}}{\rho_i}\beta_0. \tag{43}$$

These are actually conditions for the interface thickness, since all other quantities are materials parameters: the interface thickness has to remain sufficiently small for the sharp-

interface limit to be applicable. For the physical properties of ice and air, the most stringent condition arises from the heat conduction in the solid ice. With $\rho_{vs}/\rho_i \sim 5\times10^{-5}$ and our estimate of β_0 [Eq. (17)] this yields the constraint

$$W \ll 5\times10^{-7}\ \text{m to}\ W \ll 5\times10^{-5}\ \text{m}, \tag{44}$$

depending on the choice of β_0. Note that a larger W can be used for interfaces with strong kinetics. It should also be noted that similar arguments have been used previously to justify the use of the sharp-interface limit for phase-field simulations of rapid dendritic growth, which is largely dominated by interface kinetics [39].

There are two more requirements for the phase-field approach to remain valid, which are independent of the choice for the asymptotics. First, W needs to remain small compared to any local radius of curvature, $W \ll 1/\mathcal{K}$. Since a typical snow grain has a radius of $\sim10^{-4}$ m, the conditions for the sharp-interface limit are stronger by one to three orders of magnitude. Second, we also need to satisfy $\tau v_n/W \ll 1$. This condition guarantees that the phase field remains sufficiently close to its equilibrium profile for the perturbative expansion to remain valid. In fact, v_n/W is the time the interface needs to advance by a distance equal to its thickness, and the relaxation time in the phase-field equation needs to be smaller than this time scale. Using Eqs. (37) and (38) to express τ in terms of the physical parameters, this yields

$$W \ll \frac{d_0'}{\beta_0' v_n} = \frac{d_0}{\beta_0 v_n}. \tag{45}$$

Since typical interface propagation velocities during snow metamorphism are of the order 10^{-9} m s^{-1} and using estimates (14) and (17) for d_0 and β_0, this leads to

$$W \ll 10^{-6}\ \text{m to}\ W \ll 10^{-4}\ \text{m}, \tag{46}$$

again depending on the choice of β_0. This constraint yields thus an interface width that is of similar order as the one given by the sharp-interface constraint (44). Note, however, that the constraints scale in different ways with β_0. While a stronger kinetics makes it easier to satisfy the conditions for the applicability of the sharp-interface limit, it enforces a sharper interface with a faster relaxation time in order to maintain the proper front profile. It is remarkable but most likely a coincidence that for the typical conditions of snow metamorphism both constraints yield similar limits for the interface thickness.

A further consequence of these observations is that only a certain range of interface kinetics can be simulated with reasonable numerical effort. In the present work, we accept this limitation. Note, however, that these conditions may be impossible to fulfill if a more detailed description of snow metamorphism is to be developed in the future. In particular, it is anticipated that a large anisotropy of the interface kinetics is needed to properly describe the morphological features seen in snow metamorphism. If such effects are to be treated with good accuracy, a proper thin-interface limit will have to be developed.

The consistency of our approach can be tested by changing features of the model that modify the thin-interface corrections, but leave the sharp-interface limit unchanged. Indeed, we observed that the addition of the antitrapping current [36,37] to our model did not appreciably change the results; similarly, a change of the interpolation functions for the heat conductivity or the specific heat led only to small changes in the simulation results. This shows that thin-interface effects are indeed present, but subdominant as expected from the above considerations.

D. Temporal scaling of the problem

A considerable numerical challenge in simulating snow metamorphism using the above equations is the large difference between diffusional and interface-migration time scales. In fact, for an estimated pore size of $L=10^{-4}$ m, the water vapor diffusion time across the pore is given by $t_D=L^2/D_v \cong 5\times10^{-4}$ s. On the other hand, a temperature gradient of $\nabla T=100$ K m^{-1} across the pore at mean temperature $T=260$ K implies a water vapor concentration gradient of $\nabla\rho_v=1.5\times10^{-10}$ kg m^{-4}, where we have neglected curvature and kinetic effects and supposed the water vapor concentrations above the interfaces equal to $\rho_{vs}(T)$ following Eq. (3). Using the mass balance at an interface, we deduce an interface velocity of $v_n \cong 3.2\times10^{-10}$ m s^{-1}, which yields a characteristic interface migration time of $t_n=L/v_n \cong 3\times10^5$ s. In summary, we have

$$t_D/t_n \sim 1.5\times10^{-9}. \tag{47}$$

Note that the characteristic diffusion time for heat across the pore, $L^2/(\kappa_a/C_a) \cong 6\times10^{-4}$ s, is of the same order of magnitude as the water vapor diffusion time t_D, whereas the one for heat diffusion across ice, $L^2/(\kappa_i/C_i) \cong 8\times10^{-3}$ s, is one order of magnitude larger.

In numerical simulations, these estimates imply that small time steps are needed to solve the diffusion equations while a large time span has to be simulated in order to capture interface movements. Fortunately, there is a more optimistic view: snow metamorphism can be regarded as a quasi-steady-state problem, in the sense that the heat- and vapor-diffusion fields are close to their steady-state solutions on the scale of an individual microstructural feature, whereas the main time dependence arises from the motion of the interfaces. In their early modeling approach, Christon *et al.* [14] used exactly this argument and solved steady-state versions of the heat- and mass-conservation equations (5) and (7) coupled at the moving ice-air interfaces by the Stefan conditions (6) and (8), and the boundary conditions for the temperature and density field, Eqs. (10) and (11) without curvature and kinetic effects.

In a phase-field approach, this solution is not practical because replacing Eqs. (34) and (35) by their steady-state equivalents would considerably complicate the overall problem formulation. However, an alternative approach can be developed to accelerate the calculations. The quantities that limit the time step are the vapor- and heat-diffusion coefficients; we therefore would like to reduce their values (which increases the diffusion time) while keeping the interface

speeds (and hence the migration time) unchanged. Let us consider a solution to the complete problem, that is, the fields ϕ, u (or ρ_v), and T as a function of time. If the vapor-diffusion coefficient and the heat conductivities are all scaled by the same factor $0<\xi<1$ while the values of the fields remain unchanged, both the mass and the heat currents are reduced by ξ. If, in addition, the ice density and the latent heat are also scaled by ξ, the interface velocities remain unchanged; this can be deduced from the Stefan boundary conditions in the sharp-interface formulation, Eqs. (6) and (8). Furthermore, the boundary conditions for the water-vapor density and the temperature at the pore walls have to remain the same in this scaling procedure. This implies that the capillary length d_0 and the kinetic coefficient β must remain unchanged, even though physically they depend on the ice density (through the factor a^3 for d_0). In other words, the density must be scaled in the transport equations, but not in the definitions of the interfacial properties.

Of course, the time-dependent solution calculated with these rescaled coefficients is not identical to the unscaled one. However, the difference is small when the evolution is quasisteady. Indeed, in an exact steady-state, the left-hand sides of Eqs. (5) and (7) are zero, and a rescaling of the diffusion coefficients does not change the solution. As long as the relative magnitude of the time derivatives is much smaller than the factor ξ, the change induced by the scaling should be negligible. This is indeed what we find in our numerical simulations. An important point in our approach is that both fluxes are scaled by the same factor, and hence the relative magnitude of the different transport mechanisms is preserved in the scaled equations.

Since the phase-field equations are formulated in terms of the vapor concentration field u that is normalized by the ice density, the definition of u as well as the values of the capillary length d_0' and kinetic coefficient β' change under this scaling procedure $u\rightarrow u/\xi$, $d_0'\rightarrow d_0'/\xi$, and $\beta'\rightarrow\beta'/\xi$; in the phase-field model, it is sufficient to change $\lambda\rightarrow\xi\lambda$ to obtain the new values of d_0' and β'; the relaxation time τ remains unchanged. Note that, as appears from these arguments, the phase-field equation (33) is thus invariant under the scaling procedure, while in the heat- and mass-diffusion equations (34) and (35) the scaling corresponds to a simultaneous reduction of the diffusion and source terms while keeping the storage term unchanged.

It is easy to verify that the scaling does not modify the conditions for the applicability of the sharp-interface limit. In fact, since both the diffusion and the source terms are scaled simultaneously, their balance (which controls the thin-interface corrections) is not modified. Furthermore, since neither the curvature nor the interface speed are modified, the general conditions for the validity of the phase-field approach also remain unchanged. Therefore, ξ can be freely chosen provided that two conditions are fulfilled. First, the solution to the scaled problem has to remain quasisteady, which implies that we must have $t_D/(\xi t_n)\ll 1$. Second, and this is the more severe constraint, the hypothesis $\rho_i\gg\rho_{vs}$ used during the model development must remain valid. This sets a limit for the value of the scaling factor of

$$\xi > 10^{-5}. \tag{48}$$

Since the diffusion coefficients are reduced by ξ, we expect an increase of the possible time steps (and therefore a numerical speedup) of the order of $1/\xi$, which can be several orders of magnitude. Note that the values of the "physical" mass and heat fluxes have to be calculated from the density and temperature fields with the unscaled values of the diffusion coefficients.

III. RESULTS

A. Numerical considerations

We discretized the metamorphism model by finite differences in space and time. For the discretization in time, we used a fully explicit scheme for the phase-field equation (33), while we discretized the diffusion terms in the heat and mass equations (34) and (35) implicitly. We solved the two resulting systems of linear equations either by direct LU decomposition in one dimension or by a squared conjugate gradient method in two or three dimensions. We used the MPI-based numerical library PETSc [40] for the implementation. While the quantitative two-dimensional model validation has been performed on a supercomputer with up to 256 processors, the 1D and qualitative 3D results presented in this paper have been achieved on desktop computers with up to 4 processors only.

An important point is the construction of the initial conditions for the snow simulations. We usually initialize our snow metamorphism model using a structure obtained from a μ-CT scan of natural snow or an artificially created microstructure. In both cases, the structural information is provided by a binary image in one, two, or three dimensions that distinguishes between ice and air. In particular, the initial interface between ice matrix and pore space is sharp and rapidly relaxes to its equilibrium width W during the first couple of time steps. If this process is conducted using the fully coupled model of heat, mass, and phase-field equations, this phase-field diffusion is interpreted as phase changes, which leads to large-amplitude heat sources and sinks at the interfaces that can destabilize the model. For this reason, the first step of any computation consists in initializing the phase field using the binary voxel image, followed by a few iterative steps of phase-field diffusion decoupled from the heat- and mass-conservation equations. In a second step, and in order to avoid long initial transients in the heat diffusion, we solve the steady-state heat transport equation for the given boundary conditions (e.g., a warm bottom, cold top, and insulated sidewalls) on the two-phase domain defined by the previously computed relaxed phase field ϕ, but without phase change. Finally, we initialize the chemical potential field u throughout the domain by setting $u=u_{\mathrm{eq}}(\phi,T)$, using the phase field ϕ and the steady-state temperature T from the previous two steps. This completes the initialization and defines the starting point for time-step iterations using the full problem given by Eqs. (33)–(35).

B. One-dimensional model validation

We used a simple serial one-dimensional ice and pore stacking that has a pseudoanalytical solution to validate and

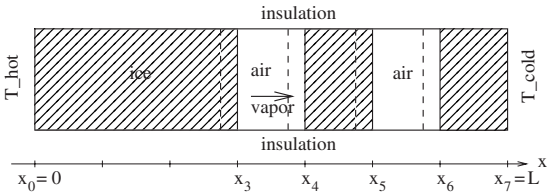

FIG. 3. Sketch of the one-dimensional experiment used to determine growth velocities. Dashed lines represent the ice surface after evolution for a certain time under an applied temperature gradient.

study the phase-field model. Consider a one-dimensional sample consisting of three ice lamellae and two pore spaces (Fig. 3), where we impose temperatures $T_0=T_{\mathrm{hot}}$ and $T_7=T_{\mathrm{cold}}$ at the boundaries to induce a temperature gradient.

1. Pseudoanalytical solution

If we suppose the problem being quasisteady with respect to the heat (and water vapor) diffusion, the temperature gradients in the ice ∇T_i and in the air ∇T_a are constant. Let us, for a moment, suppose that heat transport due to (re)sublimation and water vapor diffusion is negligible. Then, since the heat flux through the sample is constant,

$$-\kappa_i \nabla T_i = -\kappa_a \nabla T_a. \tag{49}$$

Using this equation together with the boundary conditions we can compute $\nabla T_i, \nabla T_a$ and successively the ice-air interface temperatures $\bar{T}_j, j \in \{3,4,5,6\}$. Neglecting any kinetic effects and noting that in one dimension the interface curvature $\mathcal{K}=0$, the water vapor concentrations at the ice-air interfaces are then given by $\rho_{v_j}=\rho_{vs}(\bar{T}_j)$, $j \in \{3,4,5,6\}$, which determines the water vapor gradients in the pores, $\nabla\rho_{v_{3,4}}, \nabla\rho_{v_{5,6}}$, and finally the normal interface velocities $v_{n_3}=-v_{n_4}=(1/\rho_i)D_v\nabla\rho_{v_{3,4}}$ and $v_{n_5}=-v_{n_6}=(1/\rho_i)D_v\nabla\rho_{v_{5,6}}$, where we assumed the interface normal $\hat{n}$ to point from the ice into the pores.

We use these estimates as initial condition for an iterative procedure to solve the quasi-steady-state problem considering also heat transport due to (re)sublimation, water vapor diffusion, and kinetic effects. In this more general case, Eq. (49) is no longer correct but must read

$$-\kappa_i \nabla T_i = -\kappa_a \nabla_{3,4} T_a + Q_{v_{3,4}}, \tag{50}$$

$$-\kappa_i \nabla T_i = -\kappa_a \nabla_{5,6} T_a + Q_{v_{5,6}}, \tag{51}$$

where $\nabla_{3,4}T_a$ and $\nabla_{5,6}T_a$ denote the (constant) temperature gradients in the two pores and

$$Q_{v_{3,4}} = -\frac{L_{sg}}{\rho_i} D_v \nabla \rho_{v_{3,4}}, \quad Q_{v_{5,6}} = -\frac{L_{sg}}{\rho_i} D_v \nabla \rho_{v_{5,6}} \tag{52}$$

are the heat sources due to water vapor transport and phase change. Moreover, the water vapor concentration at the ice-air boundaries will be computed using the Gibbs-Thomson equations

$$\rho_{v_j} = \rho_{vs}(\bar{T}_j)(1+\beta v_{n_j}), \quad j \in \{3,4,5,6\}. \tag{53}$$

The iterative procedure leading to a quasisteady solution then reads (1) compute $Q_{v_{3,4}}, Q_{v_{5,6}}$ from the available $\nabla\rho_{v_{3,4}}, \nabla\rho_{v_{5,6}}$ using Eq. (52); (2) compute $\nabla T_i, \nabla_{3,4}T_a, \nabla_{5,6}T_a$ using Eqs. (50) and (51), and the boundary conditions; determine new interface temperatures $\bar{T}_j$, $j \in \{3,4,5,6\}$; (3) compute ρ_{v_j}, $j \in \{3,4,5,6\}$ using the Gibbs-Thomson relations (53) and determine the new $\nabla\rho_{v_{3,4}}, \nabla\rho_{v_{5,6}}$.

If we apply this iterative procedure to a domain of length $L=5$ mm with pores at $x \in \{\frac{3}{7}L, \frac{4}{7}L\} \cup \{\frac{5}{7}L, \frac{6}{7}L\}$, temperatures $T_0=261$ K, $T_7=260$ K, thus $\nabla T=200$ K m^{-1} and for physical parameters typical for snow (see Table I) we find after a couple of iterations steady heat and mass fluxes of

$$-\kappa_i \nabla T_i = -\kappa_a \nabla_{3,4} T_a + Q_{v_{3,4}} = -\kappa_a \nabla_{5,6} T_a + Q_{v_{5,6}} = 19.091 \text{ W m}^{-2} \tag{54}$$

and

$$-D_v \nabla \rho_{v_{3,4}} = 1.970 \times 10^{-6} \text{ kg m}^{-2}, \tag{55}$$

$$-D_v \nabla \rho_{v_{5,6}} = 1.917 \times 10^{-6} \text{ kg m}^{-2}, \tag{56}$$

corresponding to normal interface velocities of

$$v_{n_{3,4}} = \mp 2.144 \times 10^{-9} \text{ m s}^{-1}, \tag{57}$$

$$v_{n_{5,6}} = \mp 2.086 \times 10^{-9} \text{ m s}^{-1}. \tag{58}$$

2. Phase-field results

Of particular interest for the model validation are the numerical convergence and the testing of the time-scaling procedure. For this, we applied the phase-field model to the 1D test case using a capillary length of $d_0=1.3\times10^{-9}$ m, all the other parameters being identical to those used for the pseudoanalytical solution.

Convergence analysis with respect to the time step Δt showed very low sensitivity as long as the solution did not exhibit numerical instabilities. Dividing an acceptable time step by two changed the simulation results only within the percentage range. As a consequence, the following simulations have been performed with $\xi\Delta t=5\times10^{-5}$ s, except for the finest discretization in space with 64000 nodes where we used $\xi\Delta t=1\times10^{-5}$ s, where ξ is the time-scaling factor.

To study the convergence with respect to space discretization, we increased successively the spatial resolution by factors of two from 2000 to 64 000 nodes (per 5 mm) while simultaneously reducing the interface thickness W from 8.0×10^{-6} m to 2.5×10^{-7} m. This guaranteed a constant numerical resolution of the interface. We let the computations evolve until the heat and mass fluxes and the interface velocities reached a quasisteady state, which was the case after

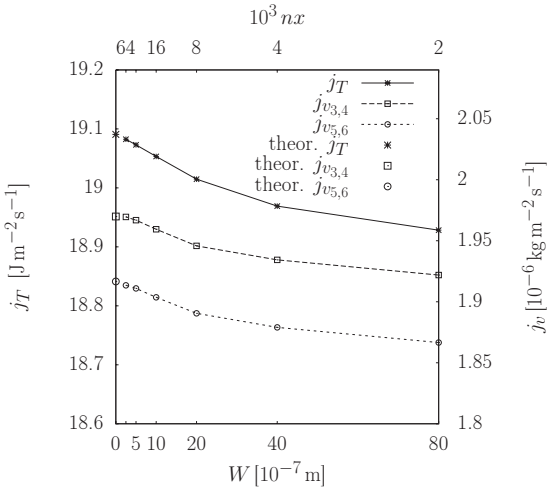

FIG. 4. Convergence with interface thickness W (respectively the number of nodes n_x) of the phase-field model to the sharp-interface results for the 1D test case, here for the model with a time-scaling factor of $\xi=10^{-3}$.

approximately 200 s (see below). Plotting the mean heat flow through the sample and the mean mass flows across the two pores (Fig. 4) shows a linear convergence in W as soon as the interface thickness is reasonably small. The fluxes converge towards values that only slightly differ from the pseudoanalytical solution.

Note that we have plotted average values, since small variations of the fluxes along the sample remained. This is due to the fact that no exact steady state can be reached since (re)sublimations at the ice-air interfaces represent small heat and mass sources and sinks that lead to slightly nonlinear temperature and solute profiles. We can thus not expect a perfect convergence to the physically approximate pseudoanalytical solution that supposes constant fluxes.

To test the time-scaling procedure and at the same time show that a quasisteady state is indeed reached, we observed the evolution of the heat and mass fluxes over time for different time-scaling factors (Fig. 5). We started the computation without scaling until a quasisteady state was reached after approximately 200 s. We then used this solution (taken at $t=300$ s) as initial condition for five computations with scaling factors varying from 10^{-1} to 10^{-5}. We also continued the nonscaled simulation for an additional 1000 s. For $\xi > 10^{-4}$, all of the results are almost identical. For $\xi=10^{-4}$, we observe that the minimum and maximum heat fluxes start to deviate from the unscaled values; for $\xi<10^{-4}$ the error becomes significant, and the minimum and maximum mass flow rates also start to evolve differently than the ones in the nonscaled simulation.

We furthermore determined ice-air interface velocities by computing the difference between the interface positions at time 1300 and 300 s and dividing by the time interval of 1000 s. Again, we observed very little influence of timescaling on the results as long as $\xi \geqslant 10^{-4}$, the variations being below the second significant digit. We computed velocities of $v_{n_{3,4}} = \mp 2.14 \times 10^{-9}$ m s^{-1} and $v_{n_{5,6}} = \mp 2.08 \times 10^{-9}$ m s^{-1}, in good agreement with the pseudoanalytical solution [Eqs. (57) and (58)].

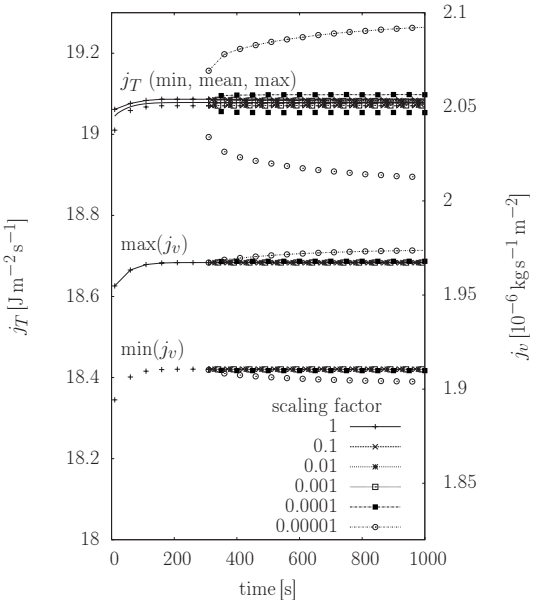

FIG. 5. Influence of the time-scaling factor ξ on the heat and mass fluxes for the one-dimensional phase-field model with an interface thickness $W=5\times10^{-7}$ m and discretization $n_x=32\,000$. Dots only represent minima, full lines mean values, and dotted lines maxima.

C. Two-dimensional bubble migration in ice

The migration of vapor figures and air bubbles through ice under a temperature gradient has first been studied by Nakaya [41]. Stehle [42] extended Nakaya's experiments and presented a study of migrating cylindrical holes at different temperatures and temperature gradients. We chose this two-dimensional setup to validate our model.

Stehle's experiments used a $2.5\times2.0\times2.0$ cm block of ice, either taken from commercial ice or made from distilled water, and usually consisting of a single crystal. A cylindrical hole with a diameter of 1 mm was drilled into the specimen, and the sample was frozen onto two copper plates on two opposing sides and isolated on the others. The mean temperature of the cylindrical hole and a temperature gradient orthogonal to the cylinder axis were controlled by setting the temperatures of the copper plates accordingly. The position of the bubble was observed with a precision of 1 μm using an optical microscope. The first position measurement and deduction of migration velocity was performed after roughly one day.

Our numerical setup represents a cut taken along the temperature gradient and orthogonal to the cylinder axis (Fig. 6). We used a 5×5 mm^2 computational domain and placed the circular hole in its center. Since the temperature field further away from the bubble is nearly undisturbed, a larger computational domain does not appreciably change the numerical results. The boundary conditions consisted of an insulation (homogeneous Neumann) at the lateral boundaries and a fixed temperature (Dirichlet) analogous to the two copper plates in the experiments at the top and bottom.

We set the phase-field parameters as before and fixed a diffuse interface thickness close to the limit for the sharp

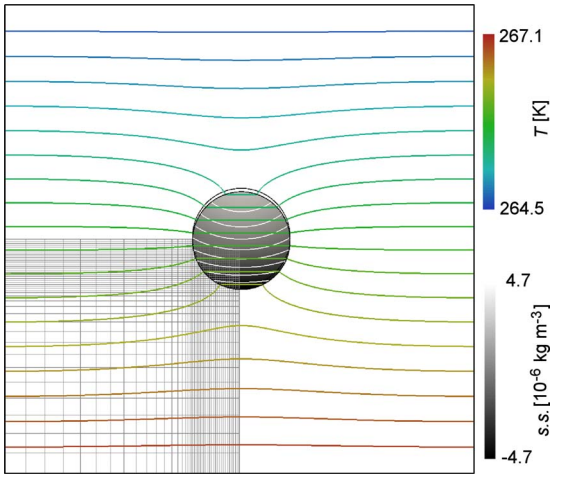

FIG. 6. (Color online) A two-dimensional bubble travels through an ice block under an imposed temperature gradient. Shown are a stylized representation of our numerical mesh (in the lower left quarter of the system), the initial bubble position, the bubble after 3 h with the supersaturation field and its isoconcentration lines within the bubble, and the isotherms across the 5×5 mm^2 ice block for experiment 3 of Stehle [42].

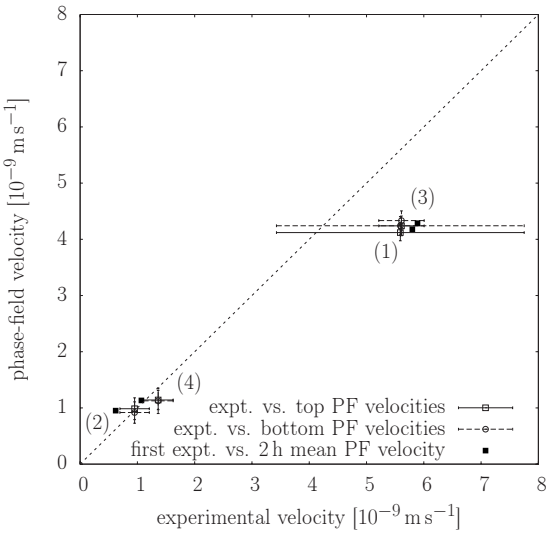

FIG. 7. Numerical versus experimental migration velocities of cylindrical holes within an ice block: mean and standard deviation of the reported experimental velocities versus the top (solid lines) and bottom (dashed lines) phase-field (PF) velocities obtained from interface positions at 1000 s intervals; the first reported experimental velocities versus the phase-field velocity obtained from the interface positions at $t=7200$ s and $t=200$ s by taking the mean of the top and bottom velocities (filled squares). The diagonal line shows a one-to-one correlation. The conditions of the experiments are (1) $T_0=264.8$ K, $\nabla T=543$ K m^{-1}, (2) $T_0=258.2$ K, $\nabla T=214$ K m^{-1}, (3) $T_0=265.8$ K, $\nabla T=520$ K m^{-1}, and (4) $T_0=271.2$ K, $\nabla T=90$ K m^{-1}.

interface approximation at $W=1\times10^{-6}$ m. For the discretization in space we defined a rectangular grid with spatial resolution $h=5\times10^{-7}$ m in the region of the bubble and coarsening gradually to $h=5\times10^{-5}$ m at the boundaries (Fig. 6), resulting in 2872^2 grid points.

Using a time-scaling factor $\xi=10^{-4}$ we let the systems evolve for at least 2 h, determined the top and bottom interface positions of the bubbles along the center-line at 200, 1200, 2200, …, 7200 s, and from these computed interface migration velocities. We compared these numerical migration velocities with the experimental ones for the four conditions published by Stehle [42] (Fig. 7). The individual computed velocities were fluctuating slightly, which is attributable to numerical noise. However, for each bubble, the top and bottom velocities were very close to each other. Moreover, no trend of increasing or decreasing velocities could be observed, suggesting that the system had reached a quasi-steady state.

For all the four experiments, our simulated velocities are within the order of magnitude of the experimental values, and the variation of the growth velocities with the parameters is correctly reproduced. A better agreement can hardly be expected. On the numerical side, sources of error are in particular the estimation of the kinetic coefficient and the capillary length, and the fact that W was chosen at the very limit of the numerical phase-field criteria. For the experimental part, we note that the problem is only approximately two-dimensional and that the cylindrical holes were on one side openly connected to the atmosphere, such that conservation of mass was *a priori* not given. Moreover, it is not unambiguously clear how the experimental bubble velocities were determined. In fact, in the experiments, not only the bubble positions but also their forms changed with time, and the bubbles started to fill with frost. We think that the velocity was determined by the position of the sublimating interface since neither the growing interface nor the center of the bubble could have been determined unambiguously. Note that, in the simulations, a vertical asymmetry in the supersaturation field is predicted, together with a very slight elongation of the bubble (e.g., for sample 3: width/height $=1.001$ after 2 h), but never as dramatic as observed by Stehle (width/height$=1.29$ after 23 h). Furthermore, our model can obviously not predict the creation of frost within the bubble because of the simplified kinetics.

D. Snow metamorphism in two and three dimensions

We performed qualitative snow metamorphism computations using μ-CT images of natural snow as the geometrical initial condition. The experimental setup to acquire the images was as follows (see also Refs. [8,9]): we prepared a snow sample by sieving natural snow (1.4 mm sieve) into a cylindrical sample holder with 4.8 cm diameter and 2.0 cm height and afterwards letting the snow sinter at a temperature of approximately -8.1 °C for a couple of hours. The resulting snow consisted of small, rounded grains (approximately 0.1 mm diameter) and had a density of 268 kg m^{-3}. We then scanned the sample with a Scanco μ-CT80 x-ray microtomograph at a resolution of 25 μm. We filtered the resulting three-dimensional gray-scale image with a Gaussian of support ±2 and standard deviation of 1 pixel in order to reduce measurement noise and successively segmented it with a gray-scale threshold such that the density (previously determined by weighting of the sample) was matched. This re-

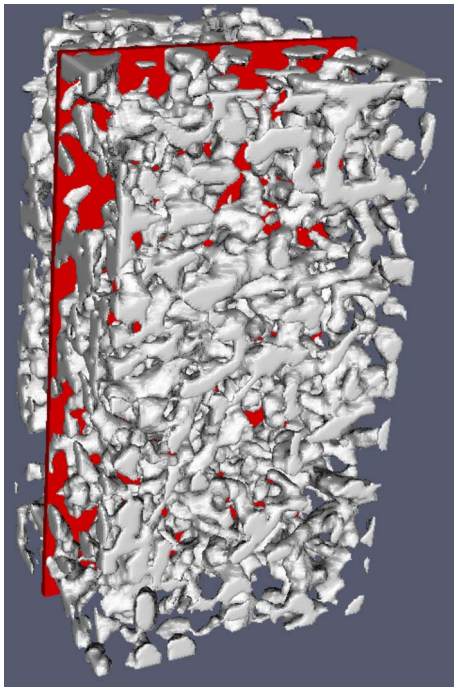

FIG. 8. (Color online) Extraction of the two-dimensional computational domain from a three-dimensional snow sample.

sulted in a three-dimensional binary image as shown in Fig. 8. To construct the computational domain, we extracted a central sub-region of $n_x \times n_y \times n_z = 100 \times 40 \times 190$ voxels (corresponding to $2.5 \times 1.0 \times 4.75$ mm), to which we added an artificial ice layer of 10 voxels at the top and bottom (in the third dimension z), leaving us with a domain of $100 \times 40 \times 210$ voxels, respectively, $2.5 \times 1.0 \times 5.25$ mm. In order to create a two-dimensional test case, we extracted the three central voxel slices across the second dimension y and projected (combined) them along y into one two-dimensional slice (Fig. 8). The reason for doing so (rather than extracting just the central slice) was to increase the ice mass and connectivity within the computational domain. The discretization in space was given by the voxel size for both the two- and the three-dimensional domains.

We imposed a fixed temperature (Dirichlet) at the top $T_{\text{top}} = 260$ K and bottom $T_{\text{bottom}} = 261$ K of the samples (in direction z) and insulation (homogeneous Neumann) at the lateral boundaries. The imposed temperature gradient was thus 190 K m^{-1}. Furthermore, we imposed no mass flow at all the boundaries, resulting in homogeneous Neumann boundary conditions for the chemical potential and phase field. This is reasonable since we expect the main flows to be oriented along the imposed temperature gradient, and since we have constructed an ice layer at the top and bottom of the computational domain.

We applied the phase-field model with the usual parameters as used for the 2D bubble migration simulations and an interface thickness of $W = 1 \times 10^{-4}$ m. Note that the sharp-interface constraints discussed in Sec. II C are violated; moreover, we used a very small time-scaling parameter $\xi = 10^{-5}$. Therefore, the results are only qualitative. Nevertheless, we can gain some insights into the heat and mass transport through a real snow microstructure. The two-dimensional simulations (Fig. 9) show that the heat flow through a snow sample is concentrating along some favored flow paths, while other regions of the snow remain nearly isothermal. Similar local effects are induced for the mass flow, such that there are some regions where sublimation or growth is favored, whereas the evolution is much slower in others.

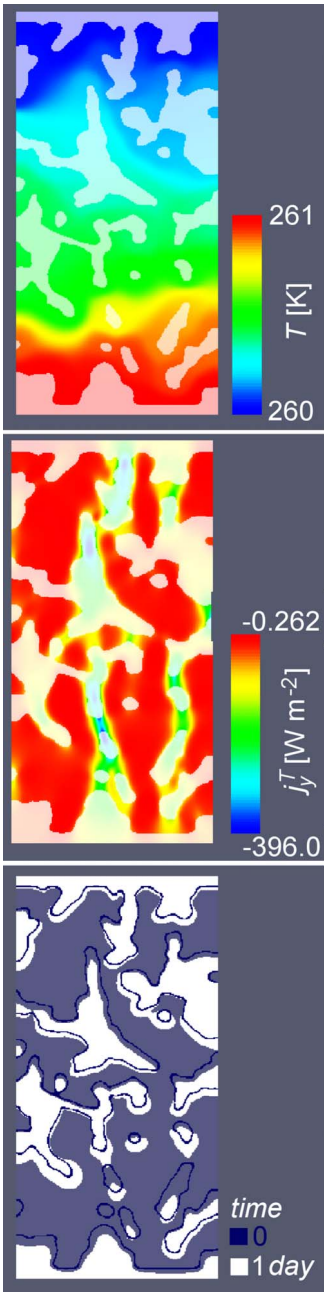

FIG. 9. (Color online) Qualitative snow metamorphism simulation in a two-dimensional slice: temperature distribution (top), heat flow (center), and structural differences (bottom) after one day under a temperature gradient of $\nabla T = 190$ K m^{-1}.

This observation can be confirmed in three dimensions (Fig. 10). The phase-field model also predicts (in both two and three dimensions) the growth of the snow grains from top to bottom, together with water vapor flow in the pores

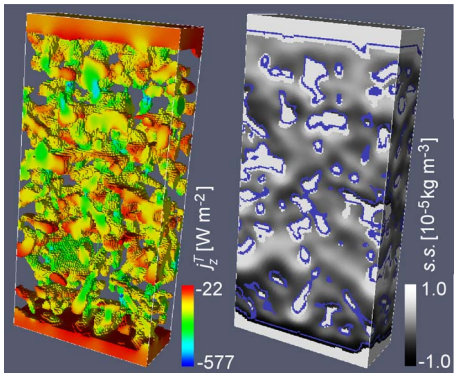

FIG. 10. (Color online) Qualitative three-dimensional snow metamorphism simulation: heat flow (left) and water vapor supersaturation field with structural differences after two days with $\nabla T = 190$ K m^{-1}.

from bottom to top (from warm to cold), which is in accordance with temperature gradient metamorphism experiments observed by μ-CT (see Fig. 1).

IV. DISCUSSION

While we have discussed most properties, simplifications, and constraints of the present approach during the model presentation in Sec. II, it is worth while to reflect on a few points in some more detail having the simulation results in mind, especially when considering future model extensions.

Our model considers heat and mass diffusion within an arbitrarily complex three-dimensional porous medium without any difficulties. The more critical part is clearly the treatment of the phase-change processes at the ice-pore interfaces, which are considerably simplified in the present work. In fact, the two interfacial parameters, the capillary length d_0 and the kinetic coefficient β, have been approximated by a constant (isotropic) value.

Concerning d_0, this choice can be justified: studies of the equilibrium form or Wulff shape of ice single crystals [43,44] suggest that d_0 is close to isotropic within the basal plane for temperatures $T > -11$ °C, the roughening temperature of the prism faces for an ice crystal in air [43], while anisotropy remains for all T with respect to the basal face: the observed equilibrium shape is either a hexagonal ($T < -11$ °C) or circular ($T > -11$ °C) plate. But theoretical estimates by Kobayashi and Kuroda [45] suggest an anisotropy of γ_{basal} versus γ_{prism} of only 1% [28], and Colbeck [43] observed that rounded spherically shaped grain forms dominate in isothermally aged snow. In any case, due to the small d_0, the influence of the surface energy term on the dynamical crystal shape is suspected to be minor for usual growth conditions.

For the kinetic coefficient β, the situation is not as favorable. In fact, the complexity of ice crystal growth [27] is believed to be mainly due to an anisotropic β that is strongly temperature dependent. The problem we face here is twofold: on the one hand, no detailed and accepted experimental or theoretical estimates of β are available; on the other hand, the introduction of an anisotropic β into the model will complicate its analysis and prevent certain simplifications. In particular, facetted growth means that the kinetic coefficient can vary by several orders of magnitude between facets and rough orientations, which makes the sharp-interface conditions [Eqs. (42) or (43)] impossible to be satisfied simultaneously for all orientations with a finite interface thickness W. In order for the phase-field model to be quantitative for such situations, a thin-interface limit will have to be developed.

For the present case with isotropic β, it would eventually also be desirable to relax the conditions on W: for the one-dimensional test case (Sec. III B) we showed that the phase-field model can reproduce accurate interface velocities when the sharp-interface constraints are satisfied. Even operating very close to the constraints, the two-dimensional bubble migration simulations reproduced trend and order of magnitudes of the experiments. For three-dimensional snow structures, however, computational costs are very high if we want to respect the sharp-interface criteria, and we have restricted the three-dimensional results within this work to qualitative analyses. Nevertheless, even such rather crude simulations allow us to gain new insights into the complexity of snow metamorphism, and first tests have shown that quantitative simulations are feasible when using massively parallel computers.

An important point that makes snow metamorphism simulations with the present phase-field method possible and attractive is the time-scaling procedure developed in Sec. II D. It allows us to increase the numerical time steps without appreciably changing the diffusion fields. Our analysis as well as all our numerical results show that we can accelerate the simulations by up to four orders of magnitude while maintaining the relevant physics of the problem.

V. CONCLUSION

We have developed a phase-field model for the simulation of temperature-gradient driven snow metamorphism. We have validated it quantitatively for simple one- and two-dimensional structures and performed qualitative simulations of metamorphism on real snow microstructures obtained by μ-CT. The simulation results are consistent with experimental observations and allow for a microstructure-based analysis of the metamorphic processes in snow.

Our model is inspired by phase-field techniques commonly used for the simulation of solidification processes and consists of (1) an asymmetric thermal diffusion equation, (2) a one-sided solute (water vapor) diffusion equation, and (3) a standard phase-field equation that is based on a double-well potential and driven by the departure of the chemical potential from its equilibrium value. An important model hypothesis is that the dominating driving forces for mass transport are the water vapor gradients in the pore space. The influence of grain boundaries, volume diffusion in ice, viscous flow, or plastic deformations is neglected. The model and its analysis are further simplified by assuming isotropic interfacial growth parameters (the capillary length and the kinetic coefficient) and by imposing a sharp-interface constraint on the diffuse interface thickness W. Furthermore, we have devel-

oped a time-scaling procedure that exploits the quasi-steady nature of the heat- and vapor-diffusion fields during snow metamorphism. This scaling procedure is crucial for the applicability of the model, since it allows us to accelerate the numerical simulations by up to four orders of magnitude.

By combining the μ-CT experiments of metamorphosing snow and the present physical model that operates at the same length scale, snow metamorphism can be studied in details not possible heretofore. This will make it possible to gain new insights into the physics of the interplay between the microstructure of the snow and its macroscopic transport properties. While the model in its present formulation is already highly useful for this purpose, it can also be extended along several lines. For instance, an extension to a multigrain model that includes more versatile sintering mechanisms is possible following the lines of Wang [46]. Furthermore, the introduction of a strongly anisotropic kinetic coefficient in conjunction with the development of a thin-interface limit (which is a nontrivial task) would make it possible to simulate facetted growth forms, such as those appearing during depth hoar formation.

ACKNOWLEDGMENTS

The computed x-ray microtomography snow images were measured in collaboration with Martin Schneebeli at the WSL Institute for Snow and Avalanche Research SLF, Davos, Switzerland. This project was funded by the U. S. Army Basic Research Terrain Properties and Processes Program and has been supported in part by an appointment to the Research Participation Program at the USACRREL administered by the Oak Ridge Institute for Science and Education through an interagency agreement between the U.S. Department of Energy and USACRREL. This work was supported in part by an allocation of computer time from the Department of Defense High Performance Computing Modernization Program at the U.S. Army Engineer Research and Development Center Major Shared Resource Center, Information Technology Laboratory, Vicksburg, Mississippi.

[1] J. Schweizer, J. B. Jamieson, and M. Schneebeli, Rev. Geophys. **41**, 1016 (2003).
[2] M. Legrand and P. Mayewski, Rev. Geophys. **35**, 219 (1997).
[3] S. A. Sokratov and R. G. Barry, J. Geophys. Res. **107**, 4374 (2002).
[4] S. A. Sokratov and R. G. Barry, J. Geophys. Res. **107**, 4093 (2002).
[5] E. M. Arons and S. C. Colbeck, Rev. Geophys. **33**, 463 (1995).
[6] J.-B. Brzoska, C. Coléou, B. Lesaffre, S. Borel, O. Brissaud, W. Ludwig, E. Boller, and J. Baruchel, Eur. Synch. Rad. Facility Newsletter **32**, 22 (1999).
[7] F. Flin, J. B. Brzoska, B. Lesaffre, C. Coléou, and R. A. Pieritz, Ann. Glaciol. **38**, 39 (2004).
[8] T. U. Kaempfer and M. Schneebeli, J. Geophys. Res. **112**, D24101 (2007).
[9] M. Schneebeli and S. A. Sokratov, Hydrolog. Process. **18**, 3655 (2004).
[10] D. A. Miller, E. E. Adams, and R. L. Brown, Cold Regions Sci. Technol. **37**, 213 (2003).
[11] M. G. Flanner and C. S. Zender, J. Geophys. Res. **111**, D12208 (2006).
[12] R. Jordan, Technical Report No. 91-16, Cold Regions Research and Engineering Laboratory, CRREL, Hanover, New Hampshire (1991).
[13] M. Lehning, P. Bartelt, B. Brown, C. Fierz, and P. Satyawali, Cold Regions Sci. Technol. **35**, 147 (2002).
[14] M. Christon, P. J. Burns, and R. A. Sommerfeld, Numer. Heat Transfer, Part A **25**, 259 (1994).
[15] F. Flin, J. B. Brzoska, B. Lesaffre, C. Coléou, and R. A. Pieritz, J. Phys. D **36**, A49 (2003).
[16] F. Flin and J. B. Brzoska, Ann. Glaciol. **49**, 17 (2008).
[17] T. U. Kaempfer, M. Schneebeli, and S. A. Sokratov, Geophys. Res. Lett. **32**, L21503 (2005).
[18] W. J. Boettinger, J. A. Warren, C. Beckermann, and A. Karma, Annu. Rev. Mater. Res. **32**, 163 (2002).
[19] L.-Q. Chen, Annu. Rev. Mater. Res. **32**, 113 (2002).
[20] G. Caginalp, Phys. Rev. A **39**, 5887 (1989).
[21] J. S. Langer, *Directions in Condensed Matter* (World Scientific, Singapore, 1986), Chap. Models of patern formation in first-order phase transitions, p. 165.
[22] A. Karma and W.-J. Rappel, Phys. Rev. E **53**, R3017 (1996).
[23] A. Karma and W.-J. Rappel, Phys. Rev. E **57**, 4323 (1998).
[24] A. Wexler, J. Res. Natl. Bur. Stand., Sect. A **81**, 5 (1977).
[25] W. J. Massman, Atmos. Environ. **32**, 1111 (1998).
[26] K. G. Libbrecht, Snowcrystals. com Web page, physical properties of ice, 1999, http://www.snowcrystals.com/ice/ice.htm
[27] T. Kobayashi, Philos. Mag. **6**, 1363 (1961).
[28] K. G. Libbrecht, Rep. Prog. Phys. **68**, 855 (2005).
[29] J. Nelson, J. Atmos. Sci. **55**, 910 (1998).
[30] V. Petrenko and R. Whitworth, *Physics of Ice* (Oxford University Press, New York, 1999).
[31] K. G. Libbrecht, Department of Physics, California Institute of Technology, Pasadena, California, 2006.
[32] J. C. Wettlaufer, Philos. Trans. R. Soc. London, Ser. A **357**, 3403 (1999).
[33] J. S. Wettlaufer and M. G. Worster, Annu. Rev. Fluid Mech. **38**, 427 (2006).
[34] R. Borcia and M. Bestehorn, Eur. Phys. J. B **44**, 101 (2005).
[35] R. F. Almgren, SIAM J. Appl. Math. **59**, 2086 (1999).
[36] B. Echebarria, R. Folch, A. Karma, and M. Plapp, Phys. Rev. E **70**, 061604 (2004).
[37] A. Karma, Phys. Rev. Lett. **87**, 115701 (2001).
[38] J. C. Ramirez, C. Beckermann, A. Karma, and H.-J. Diepers, Phys. Rev. E **69**, 051607 (2004).
[39] J. Bragard, A. Karma, Y. Lee, and M. Plapp, Interface Sci. **10**, 121 (2002).
[40] S. Balay, K. Buschelman, W. D. Gropp, D. Kaushik,

M. G. Knepley, L. C. McInnes, B. F. Smith, and H. Zhang, *PETSc Web page* (2001), http://www.mcs.anl.gov/petsc

[41] U. Nakaya, Technical Report Research Paper 13, Snow Ice and Permafrost Research Establishment, Corps of Engineers, US Army, (1956).

[42] N. S. Stehle, Technical Report Vol. R 421, US Naval Civil Engineering Laboratory, Port Huneme, California (1965).

[43] S. C. Colbeck, J. Cryst. Growth **72**, 726 (1985).

[44] M. Elbaum, Phys. Rev. Lett. **67**, 2982 (1991).

[45] T. Kobayashi and T. Kuroda, in *Morphology of crystals Part B*, edited by I. Sunagawa (Terra, Sapporo, Japan, 1987), pp. 649–737.

[46] Y. U. Wang, Acta Mater. **54**, 953 (2006).

[47] Engineering ToolBox, *Web page, Tools and Basic Information for Design, Engineering and Construction of Technical Applications*, 2005, http://www.engineeringtoolbox.com/air-properties-d_156.html

[48] The individual gas constant is the fraction of the universal gas constant R and the molecular weight of the considered gas.